Superflow passing over a rough surface: Vortex nucleation

Thomas Frisch[*] and Sergey Nazarenko[†]
Université Côte d'Azur, CNRS, Institut de Physique de Nice (INPHYNI), 06100 Nice, France

Sergio Rica[‡]
Instituto de Física, Pontificia Universidad Católica de Chile, Avenida Vicuña Mackenna 4860, Santiago, Chile

(Received 29 September 2023; accepted 19 January 2024; published 26 February 2024)

The transition from a free vortex superflow to a dissipative vortex flow in a superfluid remains an open problem, in particular because in real experiments, microscopic asperities on the walls play a major role since the relevant scales in a superfluid motion are basically of atomic scale. Here we model a superflow using the Gross-Pitaevskii mean-field equation in a domain with a rigid sinusoidal boundary. We demonstrate, analytically and numerically, the existence of a well-defined critical velocity for vortex nucleation. Additionally, we discuss the intrinsic mechanism of vortex nucleation by the appearance of a solitary wave characterized by a depletion of the wave function near the boundary.

DOI: 10.1103/PhysRevFluids.9.024701

I. INTRODUCTION

Superfluids are ubiquitous in physical systems. They were discovered first in low-temperature liquid helium [1] (see Ref. [2] for a discussion on the subject), Bose-Einstein condensates [3], nonlinear optical cavities [4,5], and exciton-polariton condensates [6]. The common properties of these systems is that the condensate phase can be described in its simplest form by a collective wave function that obeys the Gross-Pitaevskii equation [7–12] (see [13,14] for more recent developments). In this context, an inviscid flow can exist below a certain critical parameter, which depends on the geometry, the particular physical interactions between atomic constituents, and the surrounding thermodynamics parameters.

Another intriguing aspect of superfluids is the presence of topological defects such as quantized vortices, which can give rise to a rich complex dynamics such as, for example, superfluid turbulence, vortex reconnections, and wave emissions [15–19]. These vortices play an important role since they are the driving elements of the entangled vortex turbulent state, which carries deep connections with classical fluids such as the observation of a Kolmogorov spectrum in superfluid turbulence [20,21].

For topological reasons, in bulk, the total circulation of the vortices is conserved. However, when a system has a boundary, this enhances phenomena such as vortex nucleation, and the total topological charges may not be necessarily conserved, thus giving rise to a transition from a potential superflow to a vortical and dissipative flow. In particular, a mechanism for vortex nucleation and emission around a disk was highlighted in Ref. [22], and was refined in [23–26]. The proposed scenario for the transition to dissipation was confirmed experimentally [3,5,6] in different contexts.

In a superfluid helium flow, the natural presence of impurities or corrugations over the obstacle surfaces, along which the superfluid flows, is of high importance because vortices are nucleated

[*]thomas.frisch@inphyni.cnrs.fr
[†]sergey.nazarenko@inphyni.cnrs.fr
[‡]sergio.rica@uc.cl

near curved boundaries where the local flow speed exceeds a critical value. These corrugations are omnipresent and are at the origin of the observed surface roughness of any solid obstacle. The tangential and perpendicular scales of the corrugations can vary from angstrom to micrometer, they are material-dependent, and they can be characterized by classical atomic force microscopy [27] or scanning tunneling microscopy at a thinner scale [28].

Additionally, in the context of Bose-Einstein condensates, these corrugations may be achieved by optical lattices. The study of flow profile and vortices near walls is thus an active area of research, and it was shown using numerical simulations of the three-dimensional (3D) Gross-Pitaevskii equation along a disordered surface (quenched disorder) that a boundary layer develops that contains a dense turbulence layer of tangled vortex lines that continually shed vortex rings into the bulk [29]. A question of actual interest is, thus, what is the critical velocity at which a vortex nucleates as a function amplitude of the corrugation? Secondly, how does the flow profile develop spatially close to a boundary, and does it resemble the classical turbulent boundary layer, e.g., the exhibition of a "log-law of the wall"?

In this article, we study the dynamics of vortex nucleation for the simplest corrugated surface—a sinusoidal shape—in order to gain some deeper analytical insight into the criteria for vortex nucleation and vortex dynamics. The advantage of the sinusoidal shape is that it is completely defined by two parameters, namely its amplitude ϵ and its wave number α, thus it is amenable to analytical calculations. We show that at the above critical speed, which is less than the speed of sound, vortices nucleate at the boundary and propagate in the system. These vortices accumulate and create a boundary layer zone, where the local flow velocity is reduced and the vorticity (strictly speaking, the number of vortices) is increased. We first characterize analytically and numerically the critical velocity at which vortex nucleation appears as a function of the corrugations amplitude and the wave number by means of an analytical solution of the potential flow along a sinusoidal shape. Further, these estimations are also improved by a Rayleigh-Janzen expansion, which takes into account perturbatively the compressibility effects. Our results compare satisfactorily with numerical simulations. The second question of interest regarding a quantum boundary layer is briefly discussed at the end in connection to the appearance of a λ-shock structure, in correspondence with classical compressible fluids, and it will be studied in a separate publication.

The article is organized as follows. In Sec. II we review the Gross-Pitaevskii equation, its main features, and we define specifically the problem that we solve analytically and numerically. Section III concerns the understanding of the origin of the critical velocity, and we perform asymptotic expansions for the explicit value of the critical velocity in terms of the geometrical parameters. Section IV shows and discusses the numerical results, which are in agreement with our analytical predictions. We end this article with a conclusion, and we provide some future perspective.

II. BASIC MODEL AND DEFINITIONS

A. Gross-Pitaevskii equation

The adimensionalized Gross-Pitaevskii equation [7–12] reads

$$i\partial_t \Psi = -\tfrac{1}{2}\nabla^2\Psi + |\Psi|^2\Psi, \tag{1}$$

where Ψ is a complex scalar field depending on time t and a 2D (in our study) coordinate $\boldsymbol{x}$.

A remarkable characteristic of the Gross-Pitaevskii Eq. (1) is the time reversibility [if $\Psi(\boldsymbol{x}, t)$ is a solution, then $\Psi^*(\boldsymbol{x}, -t)$ is also a solution]. Moreover, the dynamics is governed by a Hamiltonian evolution with the Hamiltonian functional

$$H = \int \left(\frac{1}{2}|\nabla\Psi|^2 + \frac{1}{2}|\Psi|^4\right) d\boldsymbol{x},$$

then

$$i\frac{\partial\Psi}{\partial t} = \frac{\delta H}{\delta\Psi^*},$$

and hence the energy H is conserved.

Among other relevant features, the Gross-Pitaevskii model admits a hydrodynamical interpretation via the Madelung transformation. By setting $\Psi = \rho^{1/2}e^{i\varphi}$, we can transform (1) into

$$\partial_t\rho = -\nabla\cdot(\rho\nabla\varphi), \tag{2}$$

$$\partial_t\varphi = \frac{1}{2\sqrt{\rho}}\Delta\sqrt{\rho} - \frac{1}{2}(\nabla\varphi)^2 - \rho(\boldsymbol{x}). \tag{3}$$

Here, $\rho = |\Psi|^2$ is a density field, and

$$\boldsymbol{v} = \nabla\varphi \tag{4}$$

is the superfluid velocity field.

Equation (2) corresponds to a continuity equation for the density ρ, and Eq. (3) is a Bernoulli-like relation for the velocity potential φ. The first term on the right of Eq. (3) is called the "quantum pressure" because it vanishes in the classical limit.

Because Eqs. (2) and (3) map to a compressible fluid with a state equation,

$$p = \tfrac{1}{2}\rho^2,$$

the Gross-Pitaevskii model admits sound waves. More specifically, perturbations of density $\rho(\boldsymbol{x}, t)$ and phase $\varphi(\boldsymbol{x}, t)$ to a uniform still background, $\rho = \rho_0 = \text{const}$, $\nabla\varphi_0 = \boldsymbol{0}$, propagate as dispersive waves and the dispersion relation obeys the well-known Bogoliubov spectrum [30], which in the long-wave limit becomes acoustic with the speed of sound $c = \sqrt{\partial p/\partial\rho|_{\rho_0}} = \sqrt{\rho_0}$.

B. Gross-Pitaevskii equation in a sinusoidal channel

To model the flow in a sinuous periodic channel, we use the following domain of integration:

$$0 \leqslant x \leqslant L_x \quad \text{and} \quad y_0(x) \leqslant y \leqslant L_y,$$

where

$$y_0(x) = \epsilon\sin(\alpha x) \tag{5}$$

is the obstacle shape, L_x is the length, and L_y is the width of the channel. In Eq. (5), $\alpha = \frac{2\pi}{L_x}n$ (with n an integer) and ϵ are, respectively, the wave number and the amplitude of the corrugation. The condition for a thin obstacle imposes $\alpha\epsilon \ll 1$. The domain of integration is sketched in Fig. 1.

To model a flow, a Galilean boost with a velocity v_0 on the superflow is imposed keeping the boundary fixed. This is done by making the transformation $\Psi(x, y, t) = \psi(x, y, t)e^{iv_0x - i\frac{1}{2}v_0^2t}$. The Gross-Pitaevskii Eq. (1) reads

$$i\partial_t\psi = -iv_0\frac{\partial\psi}{\partial x} - \frac{1}{2}\nabla^2\psi + |\psi|^2\psi. \tag{6}$$

The boundary conditions (BCs) are chosen to be periodic in the x coordinates, and the wave function vanishes at $y = y_0(x)$:

$$\psi(x, y, t) = \psi(x + L_x, y, t), \tag{7}$$

$$\psi(x, y = y_0(x), t) = 0. \tag{8}$$

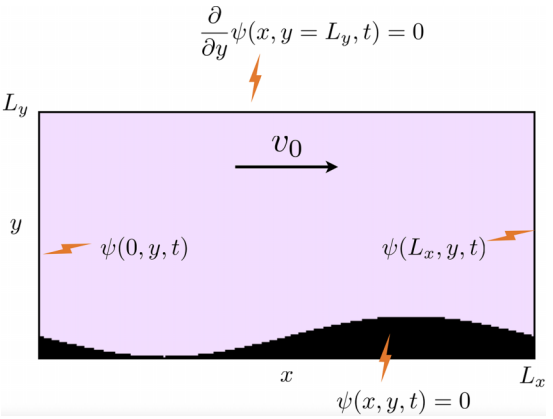

FIG. 1. Sketch of the domain of integration of the Gross-Pitaevskii Eq. (1). The bottom interface is taken as a sinusoidal profile (5). Periodic boundary conditions along the x-axis are imposed. The top boundary obeys a von Neumann boundary condition. Finally, a flow with velocity v_0 is imposed via a Galilean boost, which transforms Eqs. (1) to (6), as explained in the text.

Finally, on the top flat boundary $y = L_y$ we have a von Neumann condition:

$$\left.\frac{\partial \psi(x, y, t)}{\partial y}\right|_{y=L_y} = 0. \tag{9}$$

III. CRITICAL VELOCITY FOR VORTEX NUCLEATION

It was noticed in Ref. [22] that the striking phenomenon of vortex nucleation in the Gross-Pitaevskii equation is linked to the problem of a transonic transition. The presence of an obstacle in a uniform flow increases necessarily the local speed at certain points on the surface of the obstacle. Therefore, at some critical upstream velocity, $v_0^{(c)}$, the local speed on the surface obstacle may become supersonic. Because the Gross-Pitaevskii equation does not have any intrinsic dissipation, as is the case of shock waves in classical fluids, no such dissipation can regularize sharp gradients induced by the supersonic transition. Instead, the sharp gradients are regularized by a dispersion due to the quantum pressure presence. This leads to the creation of a dark soliton (or, for highly supersonic velocities, a train of dark solitons forming a so-called dispersive shock; see Fig. 6). It is a transverse (snaking) instability of such solitons that leads to the fact that the local density minima in the evolving soliton perturbations touch zero values, thereby creating vortices, making the fluid locally subsonic near the vortices.

In the section below, we describe carefully the mathematical treatment for the determination of the critical velocity.

A. Critical velocity condition

In Refs. [22,31], the problem of the critical velocity is reduced in the limit of zero quantum pressure to the compressible flow described by the stationary problem. This problem matches perfectly with the stationary motion of compressible fluids [32]. This analogy comes directly from (2) together with Eq. (3). The boundary conditions are $\rho(\boldsymbol{x}) \to \rho_0$ and $\nabla\varphi \to v_0\hat{\boldsymbol{x}}$ as $|\boldsymbol{x}| \to \infty$. To satisfy Eq. (3), the phase must obey

$$\varphi = -\left(\rho_0 + \tfrac{1}{2}v_0^2\right)t + \phi(\boldsymbol{x}), \tag{10}$$

where $\phi(\boldsymbol{x})$ does not depend explicitly on time, moreover $\phi(\boldsymbol{x}) \to v_0 x$ as $|\boldsymbol{x}| \to \infty$.

Neglecting the $\frac{1}{2\sqrt{\rho}}\Delta\sqrt{\rho}$ term in Eq. (3) provides a Bernoulli-like relation for $\rho(\boldsymbol{x})$ in terms of $\nabla\phi$:

$$\rho(v) = c^2 + \tfrac{1}{2}v_0^2 - \tfrac{1}{2}v^2, \tag{11}$$

with $v^2 = (\nabla\phi)^2$. Therefore, from (2) ϕ is ruled by the following nonlinear partial differential equation:

$$\nabla\cdot\left[\left(c^2 + \tfrac{1}{2}\left(v_0^2 - (\nabla\phi)^2\right)\right)\nabla\phi\right] = \mathbf{0} \quad \in \Omega, \tag{12}$$

$$\nabla\phi\cdot\hat{\boldsymbol{n}} = \mathbf{0} \quad \in \partial\Omega, \tag{13}$$

$$\nabla\phi = v_0\hat{\boldsymbol{x}} \quad \text{when} \quad y\to\infty. \tag{14}$$

Hereafter, we are considering theoretically a superfluid motion in a semi-infinite space $y > y_0(x)$ with a periodic boundary $y_0(x)$ on which $\psi(x, y, t)$ is zero. The domain used in the numerical simulation described in Fig. 1 has, for practical reasons, a finite extent in the y direction due to the finite size of the numerical simulation domain and is also periodic in the x direction.

In Eq. (13),

$$\hat{\boldsymbol{n}} = \frac{1}{\sqrt{1 + [y_0'(x)]^2}}(-y_0'(x), 1) \tag{15}$$

is the unit vector perpendicular to the interface.

As a general result, the maximum velocity $|\nabla\phi|_{\max}$ is reached on the boundary of the obstacle and in general $|\nabla\phi|_{\max} > v_0$. As v_0 increases, $|\nabla\phi|_{\max}$ increases until a critical value:

$$v_0^{(c)}, \tag{16}$$

for which the elliptic Eq. (12) becomes hyperbolic as soon as the local speed $|\nabla\phi|_{\max}$ reaches v_*, a critical velocity that will be defined in the sequel.

The criterion for the subsonic-supersonic (transonic) transition reads as follows [22]. We recall the Bernoulli-like relation (11), which links the density to the fluid velocity, and the continuity Eq. (12) implies

$$\rho(v)\nabla^2\phi + \frac{\partial\rho(v)}{\partial v}\frac{\partial_i\phi\partial_k\phi}{v}\partial_{ik}\phi = 0. \tag{17}$$

Here $v = |\nabla\phi|$, and we have used $\partial_i\rho(v) \equiv \partial_i\rho(|\nabla\phi|) = \frac{\partial\rho(v)}{\partial v}\partial_i v = \frac{\partial\rho(v)}{\partial v}\frac{v_k}{v}\partial_i v_k$, with $v_k = \partial_k\phi$, and the repeated index stands for a sum.

Writing Eqs. (17) in a diagonal form, that is, by setting a local set of variables that suppresses second-order cross derivatives, we obtain, after a straightforward calculation, an equation for ϕ and the respective boundary condition (13):

$$\rho(v)\partial_{yy}\phi + [\rho(v) + v\rho'(v)]\partial_{xx}\phi = 0, \tag{18}$$

$$\partial_y\phi - y_0'\partial_x\phi = 0. \tag{19}$$

Here we have used the fact that at the point of maximal velocity, the local frame of reference is the actual (x, y) coordinates. Equation (18) is an elliptic differential equation, but it can become hyperbolic when $[\rho(v) + v\rho'(v)]$ vanishes and changes sign for a critical value of the velocity $v = v_*$ [33]. Therefore, the local critical velocity reads [22]

$$\rho(v_*) + v_*\rho'(v_*) = c^2 + \tfrac{1}{2}v_0^2 - \tfrac{3}{2}v_*^2 = 0, \tag{20}$$

that is,

$$v_*^2 = \tfrac{2}{3}c^2 + \tfrac{1}{3}v_0^2. \tag{21}$$

Here, the local critical v_* should not be confused with the upstream critical velocity $v_0^{(c)}$, which we defined earlier in (16).

B. Solution of the incompressible flow using potential theory

1. Zeroth-order potential flow

In Ref. [22], the critical velocity has been estimated using the critical velocity conditions (21) and an inviscid incompressible approximation of the flow. Proceeding similarly, we compute the zeroth-order inviscid potential solution by using a conformal mapping. In the current situation, the zeroth-order flow may be computed approximately only. Let $f(z)$ be an analytic function:

$$f(z) = v_0(z - \epsilon e^{i\alpha z}). \tag{22}$$

By splitting the imaginary and real part of $f(z = x + iy) = \phi(x, y) + i\chi(x, y)$, each of them being harmonic functions, $\nabla^2\phi = \nabla^2\chi = 0$. We obtain the potential velocity, ϕ, and the stream function, χ. They read

$$\phi = x - \epsilon e^{-\alpha y}\cos(\alpha x) \quad \text{and} \quad \chi = y - \epsilon e^{-\alpha y}\sin(\alpha x). \tag{23}$$

The complex velocity becomes

$$u_x - iu_y = \frac{df}{dz} = v_0(1 - i\alpha\epsilon e^{i\alpha z}) \tag{24}$$

with

$$u_x = \frac{\partial\phi}{\partial x} = v_0(1 + \alpha\epsilon e^{-\alpha y}\sin(\alpha x)) \quad \text{and} \quad u_y = \frac{\partial\phi}{\partial y} = v_0\alpha\epsilon e^{-\alpha y}\cos(\alpha x).$$

The boundary is given by the stream function (23) condition $\chi(x, y_0(x)) = 0$. Thus, the interface follows the following implicit equation:

$$y_0 = \epsilon e^{-\alpha y_0}\sin(\alpha x),$$

which at first order reads

$$y_0(x) = \epsilon\sin(\alpha x) - \alpha\epsilon^2\sin^2(\alpha x) + O(\epsilon^3). \tag{25}$$

Because this is not exactly the right boundary, the conformal mapping (22) must be corrected with a term proportional to $\alpha\epsilon^2 e^{i2\alpha z}$ to eliminate the second term on the right-hand side of (25), and so forth.

Up to the first order in $\alpha\epsilon$, the local maximum speed is reached, as expected, at the maximum of deformation, namely at $\alpha x = \pi/2$, giving

$$u_x^2 + u_y^2 = v_0^2(1 + 2\alpha\epsilon).$$

Following Frisch *et al.* [22], the critical upstream velocity, $v_0^{(c)}$, up to order $\alpha\epsilon$, follows from the critical conditions given in condition (20) or equivalently (21). It gives the second-order polynomial in v_0, namely

$$c^2 + \tfrac{1}{2}v_0^2 - \tfrac{3}{2}v_0^2(1 + 2\alpha\epsilon) = 0,$$

thus

$$\frac{v_0^{(c)}}{c} = \frac{1}{\sqrt{1 + 3\alpha\epsilon}} \approx 1 - \frac{3}{2}\alpha\epsilon + O(\epsilon^2). \tag{26}$$

2. Higher-order correction in the rugosity

The computation of the higher-order in $\alpha\epsilon$ corrections for the incompressible flow is obtainable as follows. At the boundary $y = y_0(x) = \epsilon \sin(\alpha x)$, the normal velocity vanishes, $v_n = \hat{\boldsymbol{n}} \cdot \boldsymbol{\nabla}\phi = \mathbf{0}$, where $\hat{\boldsymbol{n}}$ is defined in (15).

A straightforward calculation indicates that the complex velocity potential that matches the boundary conditions up to order $(\alpha\epsilon)^3$ reads

$$f(z) = v_0\left(z - e^{i\alpha z}\left(\epsilon + \frac{\alpha^2\epsilon^3}{8}\right) + i\epsilon^2\frac{\alpha}{2}e^{2i\alpha z} + \frac{3}{8}\alpha^2\epsilon^3 e^{3i\alpha z}\right),$$

therefore the velocity potential becomes

$$\phi(x,y) = v_0\left[x - \epsilon e^{-\alpha y}\left(1 + \frac{\alpha^2\epsilon^2}{8}\right)\cos(\alpha x)\right] - \frac{1}{2}\alpha\epsilon^2 e^{-2\alpha y}\sin(2\alpha x) + \frac{3}{8}\alpha^2\epsilon^3 e^{-3\alpha y}\cos(3\alpha x). \tag{27}$$

Replacing the velocity components $u_x = \partial_x\phi(x,y)$ and $u_y = \partial_y\phi(x,y)$ in (26), the critical velocity becomes

$$v_0^{(c)} = \frac{1}{\sqrt{1 + 3\alpha\epsilon + \frac{3(\alpha\epsilon)^2}{2} - \frac{3}{4}(\alpha\epsilon)^3}},$$

thus

$$v_0^{(c)} \simeq 1 - \tfrac{3}{2}\alpha\epsilon + \tfrac{21}{8}(\alpha\epsilon)^2 - \tfrac{75}{16}(\alpha\epsilon)^3 + O((\alpha\epsilon)^4).$$

C. Rayleigh-Janzen Mach number expansion

In Ref. [31], the critical velocity was obtained by a Rayleigh-Janzen expansion in Mach number. Roughly speaking, Eq. (12) with the boundary conditions (13) and (14) is solved by a perturbation expansion in the Mach number, namely, assuming that the ratio between upstream velocity and the speed of sound is small, $M = v_0/c \ll 1$.

1. First-order correction for the compressible flow

Assume the asymptotic expansion

$$\phi(x,y) = \phi_0(x,y) + \frac{v_0^2}{c^2}\phi_1(x,y) + \cdots,$$

where $\phi_0(x,y)$ corresponds to the incompressible flow (23) already calculated up to order $O(\alpha\epsilon)^4$, and $\phi_1(x,y)$ corresponds to the first-order correction in the Mach number. Notice that because of the symmetry $\phi \to -\phi$ of Eq. (12), the Rayleigh-Janzen expansion contains only even terms in the Mach number.

The first-order correction to the basic incompressible potential flow is governed by the following linear inhomogeneous equation and its boundary conditions:

$$\nabla^2\phi_1 = -\frac{1}{2}\boldsymbol{\nabla}\cdot\left[\left(1 - \frac{(\boldsymbol{\nabla}\phi_0)^2}{v_0^2}\right)\boldsymbol{\nabla}\phi_0\right], \tag{28}$$

$$\boldsymbol{\nabla}\phi_1 \cdot \hat{\boldsymbol{n}} = 0 \quad \in \partial\Omega, \tag{29}$$

$$\boldsymbol{\nabla}\phi_1 = 0 \quad x \to \infty, \tag{30}$$

where

$$\hat{\boldsymbol{n}} = \frac{1}{\sqrt{1+(\epsilon\alpha)^2\cos^2(\alpha x)}}(-\epsilon\alpha\cos(\alpha x), 1)$$

and $\phi_0(x, y) = v_0[x - \epsilon e^{-\alpha y}\cos(\alpha x)]$ is the zeroth-order velocity potential.

The solution ϕ_1 of (28) that satisfies the boundary conditions (29) and (30), up to order $O(\alpha\epsilon)^2$, is

$$\phi_1 = -\frac{v_0}{2}\epsilon e^{-\alpha y}[\cos(\alpha x) + \alpha y\cos(\alpha x)]. \tag{31}$$

The reader may check boundary conditions are satisfied up to $O(\alpha\epsilon)$. The local speed, $v^2 = u_x^2 + u_y^2$, at the boundary $y_0(x) = \epsilon\sin(\alpha x)$ is found to be

$$v^2 = v_0^2\left(1 + 2\alpha\epsilon\sin(\alpha x) + \alpha\epsilon\frac{v_0^2}{c^2}\sin(\alpha x)\right) + O(\alpha\epsilon)^2,$$

therefore the maximum value is for $\alpha x = \pi/2$, and the maximum local speed becomes

$$v_{\max}^2 = v_0^2\left(1 + 2\alpha\epsilon + \alpha\epsilon\frac{v_0^2}{c^2}\right) + O(\alpha\epsilon)^2.$$

Using the critical condition (21), we obtain a fourth-order algebraic equation, which reads

$$\frac{3}{2}\alpha\epsilon\frac{v_0^4}{c^4} + (3\alpha\epsilon + 1)\frac{v_0^2}{c^2} - 1 = 0,$$

thus the critical velocity is found to be

$$\frac{v_0^{(c)}}{c} = \sqrt{\frac{\sqrt{1 + 12\alpha\epsilon + 9\alpha^2\epsilon^2} - 1 - 3\alpha\epsilon}{3\alpha\epsilon}} \approx 1 - \frac{9}{4}\alpha\epsilon + O((\alpha\epsilon)^2). \tag{32}$$

We underline that the first-order correction in $\alpha\epsilon$ changes from $-\frac{3}{2}\alpha\epsilon$ at order M^0, to $-\frac{9}{4}\alpha\epsilon$ at order M^2. This means that the compressibility effect is important even in the leading order in $\alpha\epsilon$.

2. Higher-order correction in the rugosity for the Rayleigh-Janzen expansion

This expansion may be pursued up to next order $O((\alpha\epsilon)^4)$ by taking as an incompressible flow the potential flow given in Eq. (27).

The solution ϕ_1 that satisfies the boundary conditions up to order $O(\alpha\epsilon)^4$ is found in the Appendix. Additionally, an expression for the maximum flow velocity is also given by Eq. (A2) in the Appendix. Using the critical condition (21), a fourth-order polynomial for v_0 is obtained:

$$3\alpha\epsilon v_0^4(4 + 8\alpha\epsilon + 3\alpha^2\epsilon^2) + v_0^2(8 + 24\alpha\epsilon + 12\alpha^2\epsilon^2 - 6\alpha^3\epsilon^3) - 8 = 0, \tag{33}$$

which leads to the long expression (A3) written in the Appendix. Here we restrict ourselves to the approximate asymptotic expansion for the critical velocity up to order three, namely

$$v_0^{(c)} = 1 - \frac{9\alpha\epsilon}{4} + \frac{279\alpha^2\epsilon^2}{32} - \frac{5937\alpha^3\epsilon^3}{128} + O((\alpha\epsilon)^4). \tag{34}$$

This critical velocity is compared with the results of the numerical simulations in Fig. 4.

D. Discussion

Although this order provides an excellent approximation for the numerical obtained values, the perturbative method must necessarily break down (see Fig. 4 below). An indication of this symptom is the substantial variation of the relevant $O(\alpha\epsilon)$ coefficient as passing from the zeroth order in Mach number (26), i.e., $-\frac{3}{2}\alpha\epsilon$, to order M^2 correction (32), i.e., $-\frac{9}{4}\alpha\epsilon$, moreover the reader may

TABLE I. Numerical parameters used in the simulation.

N_x	N_y	dx	dt	Used in figures
128	128	0.5	0.01	Fig. 3 and Fig. 4(vi) (blue)
256	256	0.5	0.01	Fig. 4(iv) (magenta)
256	256	0.25	0.0025	Fig. 6
256	256	0.125	0.001	Fig. 2, Fig. 4(v) (green), and Fig. 5
512	256	0.25	0.0025	Fig. 4(iii) (purple)
1024	256	0.25	0.0025	Fig. 4(i) (orange)
512	512	0.125	0.001	Fig. 4(ii) (red)

verify that the same coefficient up to order M^4 in the Rayleigh-Janzen perturbation scheme becomes $-\frac{27}{16}\alpha\epsilon$, suggesting a possible divergent behavior. Indeed, this sequence indicates a singular behavior in the limit $\alpha\epsilon \to 0$. For a slender obstacle, as we are considering here, the expected critical Mach number is close to unity, and therefore the Rayleigh-Janzen asymptotic expansion may break down. However, another approximation method can be realized in this case. This problem was considered by Falkovich [34] and von Kármán [35,36], and is reviewed in detail in the book by Landau and Lifshitz [32] in Sec. 126. Let us reproduce the key points of this approach.

At the transonic transition, that is, whenever the maximum local velocity satisfies $v \lesssim v_*$, the maximum speed is along the x-axis, thus $\phi = v_* x + \tilde{\phi}(x, y)$, and the equation for $\tilde{\phi}(x, y)$ admits a self-similar solution of (18) of the form

$$\tilde{\phi}(x, y) = \frac{L v_* (\alpha\epsilon)^{2/3}}{3^{1/3}} \Phi\left(\xi = \frac{x}{L}, \eta = \frac{(3\alpha\epsilon)^{1/3} y}{L}\right).$$

Finally, the expected critical velocity satisfies a singular in $\alpha\epsilon$ dependence as follows:

$$\frac{v_0^{(c)}}{c} = 1 - K(\alpha\epsilon)^{2/3}, \tag{35}$$

where K is a constant.

This peculiar similarity law is hard to verify numerically because it is pertinent only in the limit $\alpha\epsilon \to 0$. Nevertheless, as we can see in the next section, with the available numerical simulations it is shown that this law agrees satisfactorily with the numerical simulations (see Fig. 4).

IV. NUMERICAL SIMULATIONS

A. Numerical scheme

The numerical simulations were realized by solving Eq. (6) in the domain defined by Fig. 1. The domain is discretized in an $N_x \times N_y$ uniform lattice, with a mesh size dx. The Laplacian, as well as the boundary conditions (7), (8), and (9) and the interface (5), are discretized using a finite-difference method. The dynamics is simulated by solving the temporal derivatives using a Crank-Nicolson scheme, which is formally reversible. In general, we have performed numerical simulations characterized by the parameters listed in Table I. The numerical parameters are such that the numerical stability condition $\frac{dt}{2dx^2} \ll 1$ is satisfied.

The initial condition is conceived by setting $\psi(x, y) = 1$ everywhere except $\psi(x, y = y_0(x)) = 0$ at the interface. Then a healing layer is built via an energy minimization process in which a ground-state wave function is found that matches the previous boundary conditions. Next, the imposed flow is switched on by increasing slowly the upstream flow velocity from zero to v_0 at a time $T = 200$ units. Afterwards, the superflow velocity v_0 remains constant (see Fig. 2).

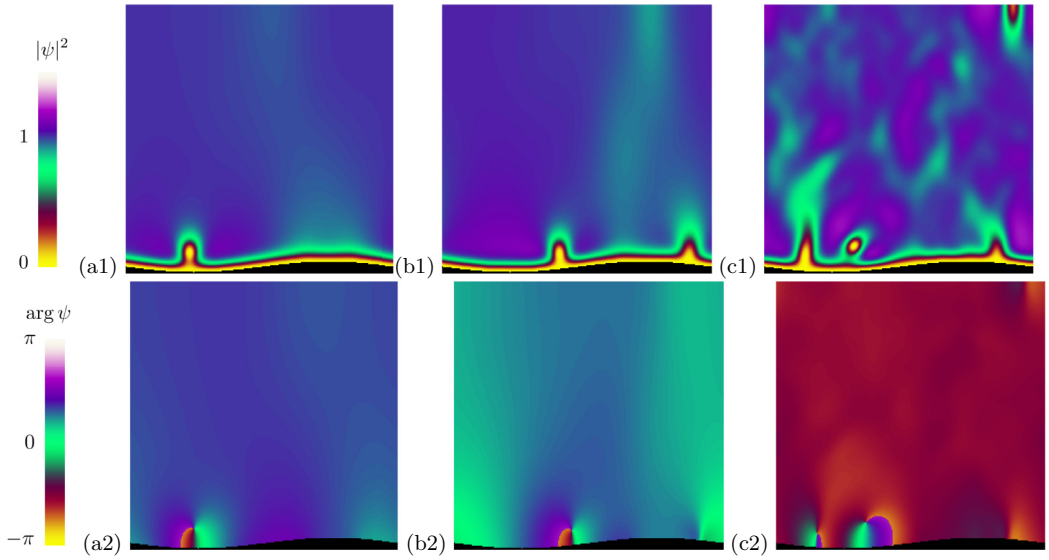

FIG. 2. Result of the numerical simulations. Snapshots for three different flow velocities. Row 1 shows the instantaneous value of $|\psi(x, y)|^2$, whereas the second row shows the phase $\phi(x, y) = \arg \psi(x, y)$. The velocities correspond to (a) $v_0 = 0.8\,c$, (b) $v_0 = 0.85\,c$, and (c) $v_0 = 0.9\,c$, and the snapshots are taken at (a) $t = 300$, (b) $t = 300$, and (c) $t = 360$. The numerical simulations are done for a system of 256^2 points, with $dx = 0.125$ and a time step $dt = 0.001$. The undulation is characterized by $\epsilon = 5dx$ and $\alpha = 2\pi/(256\,dx)$, thus $\alpha\epsilon = 0.1227$.

B. Measurement of the "vorticity"

In the Gross-Pitaevskii model, there is no formal way to define a vorticity field. The usual definition in fluid dynamics does not provide a regular field. Nevertheless, a possible regularized representation of the vorticity can be done by taking the curl of the superfluid current,

$$\boldsymbol{j} = \frac{1}{2i}(\bar{\psi}\boldsymbol{\nabla}\psi - \psi\boldsymbol{\nabla}\bar{\psi}) = \rho\boldsymbol{\nabla}\varphi. \tag{36}$$

The vorticity thus reads [16]

$$\boldsymbol{\omega}^* = \frac{1}{2}\boldsymbol{\nabla}\times\boldsymbol{j} = \frac{1}{2i}\boldsymbol{\nabla}\bar{\psi}\times\boldsymbol{\nabla}\psi = \frac{1}{2}\boldsymbol{\nabla}\rho\times\boldsymbol{\nabla}\phi. \tag{37}$$

In two space dimensions, $\boldsymbol{\omega}^*$ is perpendicular to the plane, namely $\boldsymbol{\omega}^* = \omega^*\hat{z}$. Moreover, because the vortex solution of the Gross-Pitaevskii equation behaves as $\rho(r) \sim r^2$, the field $\omega^*(x, y)$ is roughly constant at the vortex core with a sign given by the topological charge or circulation of the vortex. Additionally, the current vorticity field decreases as $1/r^4$ as $r > \xi_0$. Therefore, ω^* represents qualitatively a vorticity-like field. However, the field $\boldsymbol{\omega}^*(x, y)$ does not seem to lead to any interesting interpretation. Its value seems to be purely phenomenological, and we shall use it because it provides a simple global quantifier of total vorticity.

The numerical calculation of $\omega^* = \frac{1}{2i}(\partial_x\bar{\psi}\partial_y\psi - \partial_y\bar{\psi}\partial_x\psi)$ is direct and provides a real field and numerically is a well-behaved quantity (see Fig. 3). In what follows, we define the following integral functional:

$$\Omega^{(2)} = \int_{\mathbb{R}^2} [\omega^*]^2\,dx\,dy. \tag{38}$$

For an isolated vortex in an infinite system, this integral is found to be approximately 0.857 564. However, due to rigid boundary conditions on the bottom wall, we have found that the integral $\Omega^{(2)}$

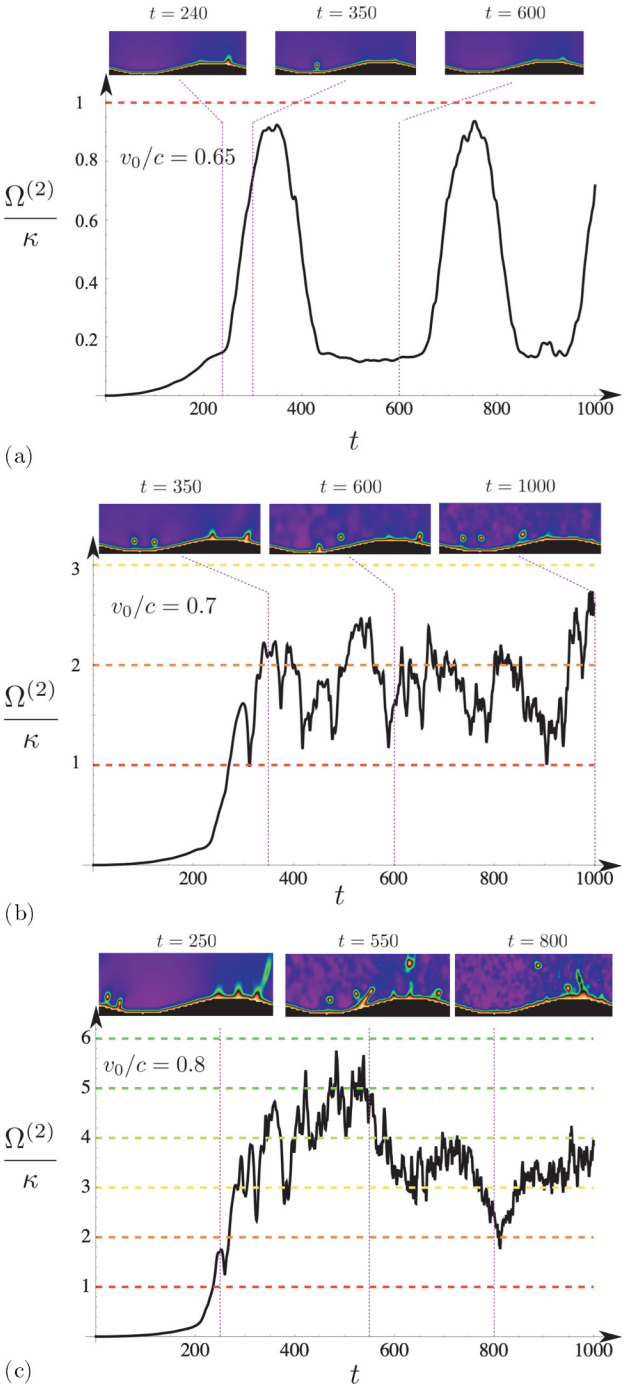

FIG. 3. Plot of the quantity $\Omega^{(2)}/\kappa$ vs time for three distinct flow velocities: (a) for $v_0 = 0.65$; (b) for $v_0 = 0.7$; and (c) for $v_0 = 0.8$. Each plot contains three snapshots of the superfluid density $|\psi|^2$ in the space near the undulated profile. The corresponding times of the snapshot are shown by a vertical segmented purple line. The numerical simulations are done for a system of 128^2 points, with $dx = 0.5$ and a time step $dt = 0.01$. The undulation is characterized by $\epsilon = 5\,dx$ and $\alpha = 2\pi/(128\,dx)$, thus $\alpha\epsilon = 0.245$. Additionally, we add for each case a movie displaying the vortex nucleation dynamics in the Supplemental Material [37].

is about $\kappa \approx 1.55$ when there is only one vortex in the system. Therefore, we conclude that the number of vortices is roughly a measure of $\Omega^{(2)}/\kappa$. This method was investigated in Fig. 3, where $\Omega^{(2)}(t)/\kappa$ is drawn versus time for three distinct flow velocities.

As is seen clearly in Fig. 3(a), near the critical velocity, $\Omega^{(2)}$ oscillates from a small value up to a constant of the order of the unit. The observed oscillation appears naturally because in the valley of the sinusoidal profile the vortex is well separated from the solid boundary having a clear and neat identity. However, when the vortex passes near the top of the sinusoidal profile, the vortex merges into the solid boundary, becoming a kind of solitary wave, hence contributing significantly less than the single vortex contribution to $\Omega^{(2)}$. For larger velocities, as soon as vortices are nucleated, the quantity $\Omega^{(2)}$ becomes larger than zero, making a fluctuating pattern for the number of vortices appear, as seen in Figs. 3(b) and 3(c). This behavior indicates an onset of a complex vortex dynamics.

It may be noticed that along the three sections in Fig. 3, there is a close agreement between the number of observed vortices and the value of the integral $\Omega^{(2)}/\kappa$.

C. Critical velocity

We have performed a large set of numerical simulations for various system sizes, various parameters α and ϵ, and various discrete dx and dt parameters for the numerical simulations, and we conclude that the critical velocity must depend on the parameter combination $\alpha\epsilon$ as expected from the theory developed in Sec. III.

The estimation of the critical velocity comes from the establishment of a lower bound critical velocity, $v_c^{(-)}$, such that for all superflow velocities $v < v_c^{(-)}$ the system does not present any vortex at any time in the volume. Additionally, we compute an upper bound velocity $v_c^{(+)}$ such that the system displays vortices at least at some time.

Figure 4 shows the data for three different values of the couple (dx, dt), as given in Table I. Additionally, we compare the curves with the first-order critical velocity (26), the third-order Rayleigh-Janzen critical velocity (34) [or (A3) in the Appendix], and the Falkovich–von Kármán theory [Eq. (35)]. The results are presented in a standard plot [Fig. 4(a)] and in a log-log plot [Fig. 4(b)] to appreciate the agreement with the Falkovich–von Kármán law (35). Although the standard plot [Fig. 4(a)] shows that the critical velocities do not depend strongly on the system size and on the discretization parameters (dx, dt), the log-log plot [Fig. 4(b)] indicates that for $\alpha\epsilon \ll 1$ the dispersion of the data increases. We note that the critical velocity slightly decreases as the system size increases. However, as the theory indicates, in the limit of infinite system size the critical velocity is finite.

D. Vortex nucleation

Although the criterium for the critical velocity of vortex nucleation described in Sec. III is very accurate, and works perfectly in all studied cases, the precise dynamical mechanism of the transition from a free-vortex stationary solution of the Gross-Pitaevskii Eq. (6) to a dynamical vortical state is still unknown. The current interpretation is that the nonlinear effects, present in the compressible fluid Eq. (18), make a spontaneously sharp gradient of the phase ϕ. This strong gradient implies through Eq. (11) a depletion of the amplitude. Such a depletion corresponds roughly to an exact solution of the Gross-Pitaevskii Eq. (6): the dark soliton found by Kuznetsov and Turitsyn [38]. Moreover, as shown in Ref. [38], this dark-soliton solution is unstable along the transverse direction. This snakelike instability leads to the appearance of another special kind of solution of the Gross-Pitaevskii Eq. (6): the Jones-Roberts [39] solitary wave. This is a family of traveling waves that matches with the solution of a traveling pair of vortices. This scenario of vortex nucleation was observed numerically by Josserand and Pomeau [40] and studied in more detail by Berloff and Roberts [41]. However, in the current case the existence of the solid boundary that imposes $\psi = 0$ makes substantial modifications. In particular, the dark-soliton solution that vanishes on a boundary

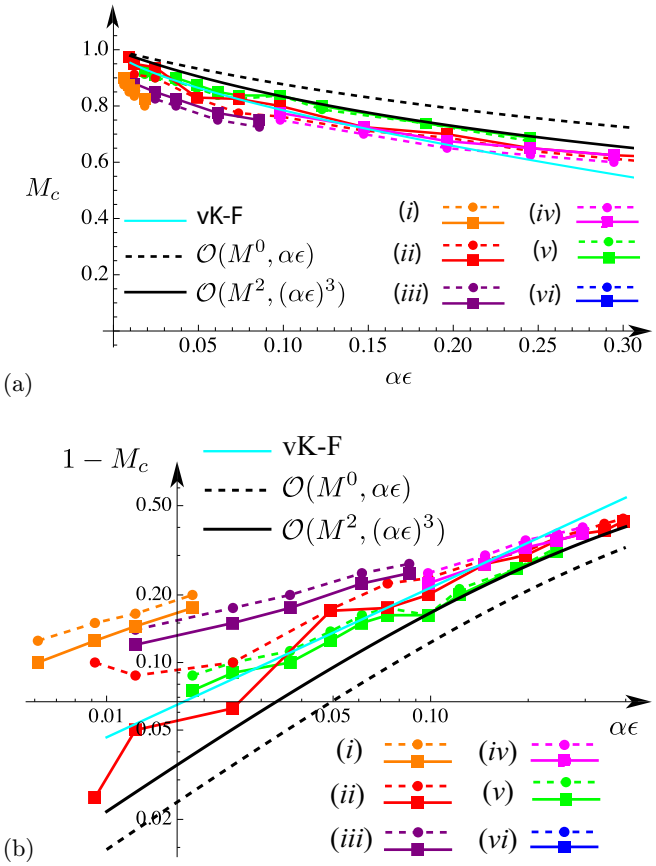

FIG. 4. Critical Mach number as a function of $\alpha\epsilon$. (a) Plots $M_c = v_0^{(c)}/c$ vs $\alpha\epsilon$ in linear scale, and (b) plots $1 - M_c$ vs $\alpha\epsilon$ in log-log scale. The numerical simulations provide the lower bound $v_c^{(-)}/c$ critical Mach number (segmented line) and the upper bound $v_c^{(+)}/c$ critical Mach number (continuous line) for different numerical parameters accordingly to Table I: (i) $dx = 0.25$ and $N_x = 1024, N_y = 256$ (orange); (ii) $dx = 0.125$ and $N_x = N_y = 512$ (red); (iii) $dx = 0.25$ and $N_x = 512, N_y = 256$ (purple); (iv) $dx = 0.5$ and $N_x = N_y = 256$ (magenta); (v) $dx = 0.125$ and $N_x = N_y = 256$ (green); and (vi) $dx = 0.5$ and $N_x = N_y = 128$ (blue). Additionally, the data are compared with three theoretical curves: the cyan curve corresponds to Falkovich–von Kármán theory [Eq. (35)], the black segmented curve corresponds to the first-order critical velocity (26), and the full black curve corresponds to the third-order Rayleigh-Janzen critical velocity (A3).

does not admit (to our knowledge) an exact solution. Additionally, the snake instability differs due to the presence of the boundaries, and finally, the Jones-Roberts structures with a boundary condition $\psi = 0$ formally do not exist.

Nevertheless, the numerical simulations show a large depletion of the amplitude of the wave function near the boundary, and more importantly the nucleation of an "embryo" traveling against the flow, which may correspond to a Jones-Roberts type of solution with a vanishing wave function near a boundary. This solution balances the effects resulting from the transonic transition and dispersion due to quantum pressure. This embryo is observed for flat corrugations, and it persists in time as long as our simulations run. Figure 5 shows the density, $|\psi|^2$, and the phase of this "embryo." Sometimes, the embryo detaches from a "crest" of the corrugation, becoming then a vortex during the travel time passing a "valley" of the corrugation. Later as the vortex approaches a new crest, it may be reabsorbed by the boundary becoming an embryo again, and so on, as shown in Fig. 3.

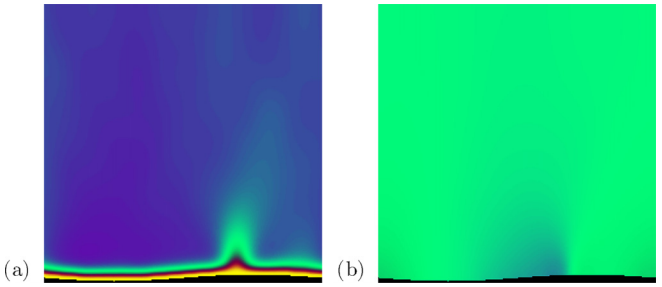

FIG. 5. Results of numerical simulations. Snapshots of the embryo at $t = 300$ time units. (a) $|\psi(x, y)|^2$ and (b) $\arg \psi(x, y)$. The modulus shows a slight depletion near the boundary, and the phase of the wave function (b) shows a step phase gradient emulating a shock wave. The simulations were done for $dx = 0.125$, $N_x = N_y = 256$, a flow velocity $v_0 = 0.8375$, $\epsilon = 3dx = 0.375$, $\alpha = \frac{2\pi}{N_x\, dx} = 0.196\,35$, and $\alpha\epsilon = 0.0736$.

Although, this "embryo" is believed to be the prevortex state, in the situation presented in Fig. 5, it does not evolve into a vortex solution for the time of our numerical simulations (about 1500 time units). Therefore, we have reasons to believe that this embryo is stable. This embryo, which consists in a depletion zone, lies perpendicularly to the obstacle and has a width that is of the order of the healing length because it is determined by the effect of quantum pressure, but it has a finite spatial extension in the y direction. As the flow velocity is increased, this extension size increases and could suffer a snaking instability leading to the formation of vortices [see Figs. 6(b1) and 6(c1)].

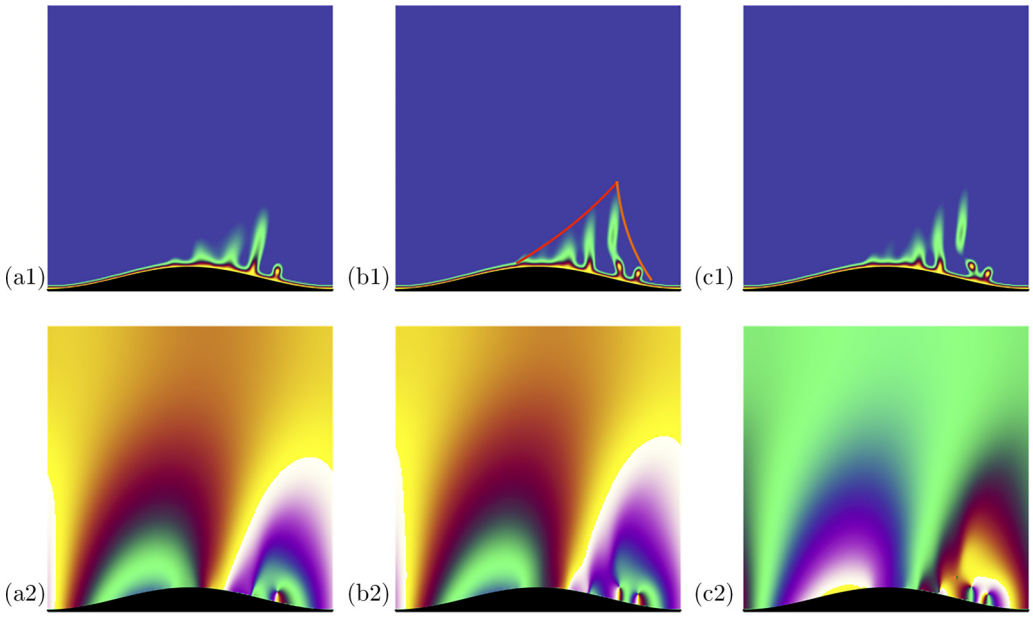

FIG. 6. Result of the numerical simulations for the anatomy of the vortex nucleation process. Snapshots for three different times for a flow velocity $v_0 = 0.85$. Row 1 shows the instantaneous value of $|\psi(x, y)|^2$, whereas the second row shows the phase $\phi(x, y) = \arg \psi(x, y)$. The time instants correspond to (a) $t = 232.5$, (b) $t = 242.5$, and (c) $t = 245$. In the snapshot (b1) we sketch the forefront in red and the backfront in orange. The numerical simulations are done for a system of 256^2 points, with $dx = 0.25$ and a time step $dt = 0.0025$. The undulation is characterized by $\epsilon = 10dx$ and $\alpha = 2\pi/(256\, dx)$, thus $\alpha\epsilon = 0.2455$.

The superflow behavior near the boundary for higher velocities, but still in the subsonic regime, is shown in Fig. 6. This regime displays several interesting aspects regarding the shock-wave interaction with a boundary. In Fig. 6(b1) we highlighted by a sketch the formation of a λ-shock pattern induced by the appearance of a wave train near the boundaries [also present in Fig. 6(c1)]. This λ-shock pattern is similar to the λ-shock structures arising in supersonic flows over bumped boundaries in classical gas dynamics [42]. The forefront [red line in Fig. 6(b1)] manifests the usual oblique shock, at an angle $\sin\alpha = v_*/v$, where v is the local speed and v_* is the local critical speed (21), whereas the backfront [orange line in Fig. 6(b1)] represents a trailing shock. In the upper region, between the two shocks, the flow is locally supersonic, and due to the dispersion relation, the local density $|\psi|^2$ admits a periodic modulation, while the downstream region is subsonic and dominated by the creation of several vortices. These vortices coexist with the embryos and are advected downstream by the flow until they detach into the main flow.

V. CONCLUSION AND PERSPECTIVE

In this article, we have investigated analytically and numerically the dynamics of the formation of vortices in a superfluid moving in a two-dimensional corrugated channel using the Gross-Pitaevskii equation. The channel corrugation consists of a sinusoidal perturbation that is simply generated by two parameters, the amplitude and the wavelength of the undulation of the channel wall. As we have increased the velocity of the incoming flow into the channel, we have observed a transition from a laminar flow, free of vortices, to a vortical flow. This transition takes place for a critical velocity that is less than the speed of sound and occurs abruptly as we increase the velocity of the flow. We have found that vortex nucleation takes place at the apex of perturbation where the local velocity is increased and that this mechanism is responsible for the injection of vorticity into the system. Furthermore, we have computed analytically and numerically the critical velocity at which vortex nucleation appears as a function of the corrugation amplitude and wave number. Our analytical results are satisfactory compared with our numerical simulations and are summarized in a phase diagram that is parametrized by the Mach number and the corrugation nondimensional parameter. Our analytical results are also improved by a Rayleigh-Janzen expansion, which takes into account in a perturbative way the compressibility effects. Finally, slightly above the critical velocity, we have observed a regime in which vortices appear and disappear as they travel along the sinusoidal wall. This regime is characterized by a measurement of the spatial integral of the square of the pseudovorticity, which is found to be a good indicator of the presence or absence of vortices.

Our work opens new perspectives on the hydrodynamics of superfluid along rough walls and/or walls with a specific shape. In particular, we expect as we increase the velocity of the incoming flow that a turbulent boundary layer due to the accumulation of vortices near the wall will be created. We plan to use larger-scale simulations and develop theoretical tools to investigate the formation of wall turbulence in superfluid, and we hope this study will motivate new experimental studies in superfluid and quantum turbulence. This kind of scenario has been studied by Stagg *et al.* [29] in three space dimensions, where roughness and impurities nucleate half vortex rings, which are advected and stretched by the flow, increasing the total vorticity length and creating a vortex tangle near the wall.

ACKNOWLEDGMENT

S.R. acknowledges partial founding from the Fédération Doeblin and FONDECYT (Chile) under Grant No. 1220369.

APPENDIX

In this Appendix, we provide the formal expressions of the intermediate perturbative calculations explained in the main text.

Starting from the asymptotic potential flow given in Eq. (27), and introducing it as $\phi_0(x, y)$ into (28), the solution for $\phi_1(x, y)$ that satisfies the boundary conditions (29) and (29), up to order

$O((\alpha\epsilon)^4)$, is

$$\phi_1(x,y) = v_0\Bigg[\frac{7}{48}\alpha^2\epsilon^3 e^{-3\alpha y}\cos(3\alpha x) + e^{-\alpha y}\left(\frac{3\alpha^2\epsilon^3}{16} - \frac{\epsilon}{2}\right)\cos(\alpha x) - \frac{1}{2}\alpha^2 y\epsilon^2 e^{-2\alpha y}\sin(2\alpha x)$$
$$+ \frac{1}{16}e^{-3\alpha y}(-\alpha^3 y\epsilon^3 e^{2\alpha y}\cos(\alpha x) + 9\alpha^3 y\epsilon^3\cos(3\alpha x) + 2\alpha^2\epsilon^3\cos(\alpha x))$$
$$-\frac{1}{4}\alpha\epsilon^2 e^{-2\alpha y}\sin(2\alpha x) - \frac{1}{2}\alpha y\epsilon e^{-\alpha y}\cos(\alpha x)\Bigg]. \tag{A1}$$

The local velocity may be computed directly. As expected, its maximum value is for $\alpha x = \pi/2$. After a straightforward calculation, we obtain

$$v_{\max}^2 = v_0^2\left(1 + 2\alpha\epsilon + \alpha^2\epsilon^2 - \frac{1}{2}\alpha^3\epsilon^3\right) + v_0^4\left(\alpha\epsilon + 2\alpha^2\epsilon^2 + \frac{3\alpha^3\epsilon^3}{4}\right) + O(\alpha\epsilon)^4. \tag{A2}$$

The formal expression for the critical velocity comes after the condition (33), which provides a fourth-order polynomial, the relevant solution of which is

$$v_0^{(c)} = \sqrt{\frac{3\alpha^3\epsilon^3 - 6\alpha^2\epsilon^2 + \sqrt{9\alpha^6\epsilon^6 - 36\alpha^5\epsilon^5 - 36\alpha^4\epsilon^4 + 192\alpha^3\epsilon^3 + 384\alpha^2\epsilon^2 + 192\alpha\epsilon + 16} - 12\alpha\epsilon - 4}{3\alpha\epsilon(3\alpha^2\epsilon^2 + 8\alpha\epsilon + 4)}}. \tag{A3}$$

[1] P. Kapitza, Viscosity of liquid helium below the λ-point, Nature (London) **141**, 74 (1938).
[2] S. Balibar, The discovery of superfluidity, J. Low Temp. Phys. **146**, 441 (2007).
[3] C. Raman, M. Köhl, R. Onofrio, D. S. Durfee, C. E. Kuklewicz, Z. Hadzibabic, and W. Ketterle, Evidence for a critical velocity in a bose-einstein condensed gas, Phys. Rev. Lett. **83**, 2502 (1999).
[4] Y. Pomeau and S. Rica, Diffraction non linéaire, C. R. Acad. Sci. Paris **397**, 1287 (1993).
[5] C. Michel, O. Boughdad, M. Albert, P.-E. Larré, and M. Bellec, Superfluid motion and drag-force cancellation in a fluid of light, Nat. Commun. **9**, 2108 (2018).
[6] A. Amo, S. Pigeon, D. Sanvitto, V. G. Sala, R. Hivet, I. Carusotto, F. Pisanello, G. Leménager, R. Houdré, E. Giacobino, C. Ciuti, and A. Bramati, Polariton superfluids reveal quantum hydrodynamic solitons, Science **332**, 1167 (2011).
[7] E. P. Gross, Unified theory of interacting bosons, Phys. Rev. **106**, 161 (1957).
[8] E.P Gross, Classical theory of boson wave fields, Ann. Phys. **4**, 57 (1958).
[9] E. P. Gross, Structure of a quantized vortex in boson systems, Nuovo Cimento **20**, 454 (1961).
[10] E. P. Gross, Hydrodynamics of a superfluid condensate, J. Math. Phys. **4**, 195 (1963).
[11] V. L. Ginzburg and L. P. Pitaevskii, On the theory of superfluidity, Sov. Phys. JETP **7**, 858 (1958).
[12] L. P. Pitaevskii, Vortex lines in an imperfect bose gas, Sov. Phys. JETP **13**, 451 (1961).
[13] L. Pitaevskii and S. Stringari, *Bose-Einstein Condensation and Superfluidity* (Oxford University Press, Oxford, 2016).
[14] A. J. Leggett, *Quantum Liquids: Bose Condensation and Cooper Pairing in Condensed-Matter Systems* (Oxford University Press, New York, 2006).
[15] R. J. Donnelly, *Cambridge Studies in Low Temperature Physics: Quantized Vortices in Helium II* (Cambridge University Press, Cambridge, England, 1991).
[16] A. Villois, G. Krstulovic, D. Proment, and H. Salman, A vortex filament tracking method for the Gross-Pitaevskii model of a superfluid, J. Phys. A **49**, 415502 (2016).
[17] S. Rica, Self-similar vortex reconnection, C. R. Mec. **347**, 365 (2019), Patterns and dynamics: homage to Pierre Coullet.
[18] A. Villois, D. Proment, and G. Krstulovic, Irreversible dynamics of vortex reconnections in quantum fluids, Phys. Rev. Lett. **125**, 164501 (2020).

[19] C. F. Barenghi, L. Skrbek, and K. R. Sreenivasan, *Quantum Turbulence* (Cambridge University Press, Cambridge, England, 2023).
[20] C. F. Barenghi, L. Skrbek, and K. R. Sreenivasan, Introduction to quantum turbulence, Proc. Natl. Acad. Sci. USA **111**, 4647 (2014).
[21] Y. Zhu, B. Semisalov, G. Krstulovic, and S. Nazarenko, Direct and inverse cascades in turbulent bose-einstein condensates, Phys. Rev. Lett. **130**, 133001 (2023).
[22] T. Frisch, Y. Pomeau, and S. Rica, Transition to dissipation in a model of superflow, Phys. Rev. Lett. **69**, 1644 (1992).
[23] C. Josserand, Y. Pomeau, and S. Rica, Vortex shedding in a model of superflow, Physica D **134**, 111 (1999).
[24] T. Winiecki, J. F. McCann, and C. S. Adams, Pressure drag in linear and nonlinear quantum fluids, Phys. Rev. Lett. **82**, 5186 (1999).
[25] C. Huepe and M.-E. Brachet, Scaling laws for vortical nucleation solutions in a model of superflow, Physica D **140**, 126 (2000).
[26] C.-T. Pham, C. Nore, and M.-É. Brachet, Boundary layers and emitted excitations in nonlinear Schrödinger superflow past a disk, Physica D **210**, 203 (2005).
[27] G. Binnig, C. F. Quate, and C. Gerber, Atomic force microscope, Phys. Rev. Lett. **56**, 930 (1986).
[28] G. Binnig and H. Rohrer, Scanning tunneling microscopy—from birth to adolescence, Rev. Mod. Phys. **59**, 615 (1987).
[29] G. W. Stagg, N. G. Parker, and C. F. Barenghi, Superfluid boundary layer, Phys. Rev. Lett. **118**, 135301 (2017).
[30] N. N. Bogolyubov, On the theory of superfluidity, J. Phys. (USSR) **11**, 23 (1947).
[31] S. Rica, A remark on the critical speed for vortex nucleation in the nonlinear Schrödinger equation, Physica D **148**, 221 (2001).
[32] L. D. Landau and E. M. Lifshitz, *Fluid Mechanics, Second Edition: Volume 6 (Course of Theoretical Physics)* (Butterworth-Heinemann, Oxford, 1987).
[33] Although $\rho(v)$ may also change sign, in our case of interest, $[\rho(v) + v\rho'(v)]$ changes sign first.
[34] S. V. Falkovich, On the theory of the laval nozzle: Translation of "k teorii sopla lavala" prikladnaya matematika i mekhanika, Vol. 10 (1946), p. 1644; NACA Technical Memorandum 1212 (1949).
[35] T. von Kármán, *The Problem of Resistance in Compressible Fluids* (Reale Accademia d'Italia, Rome, 1935).
[36] T. von Kármán, The similarity law of transonic flow, J. Math. Phys. **26**, 182 (1947).
[37] See Supplemental Material at http://link.aps.org/supplemental/10.1103/PhysRevFluids.9.024701. for a movie of a longtime evolution of the nucleation process.
[38] E. A. Kuznetsov and S. K. Turitsyn, Instability and collapse of solitons in media with a defocusing nonlinearity, JETP **67**, 1583 (1988).
[39] C. A. Jones and P. H. Roberts, Motions in a bose condensate. IV. Axisymmetric solitary waves, J. Phys. A **15**, 2599 (1982).
[40] C. Josserand and Y. Pomeau, Generation of vortices in a model of superfluid 4He by the kadomtsev-petviashvili instability, Europhys. Lett. **30**, 43 (1995).
[41] N. G. Berloff and P. H. Roberts, Motions in a Bose condensate: X. New results on the stability of axisymmetric solitary waves of the Gross-Pitaevskii equation, J. Phys. A **37**, 11333 (2004).
[42] M. Gramola, P. J. K. Bruce, and M. Santer, Experimental FSI study of adaptive shock control bumps, J. Fluids Struct. **81**, 361 (2018).